



Fast X-ray microfluorescence imaging with submicrometer-resolution integrating a Maia detector at beamline P06 at PETRA III

Ulrike Boesenberg,^{a*} Christopher G. Ryan,^b Robin Kirkham,^b D. Peter Siddons,^c Matthias Alfeld,^a Jan Garrevoet,^a Teresa Núñez,^a Thorsten Claussen,^a Thorsten Kracht^a and Gerald Falkenberg^a

Received 17 May 2016

Accepted 28 September 2016

Edited by G. E. Ice, Oak Ridge National Laboratory, USA

Keywords: Maia detector; X-ray fluorescence; micro-XRF.

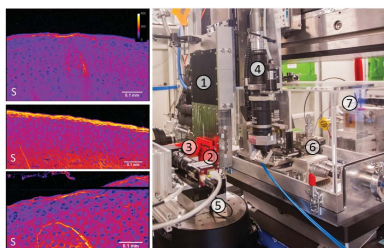
^aDeutsches Elektronen Synchrotron (DESY), Notkestrasse 85, 22607 Hamburg, Germany, ^bCommonwealth Scientific and Industrial Research Organisation (CSIRO), Clayton, Victoria, Australia, and ^cBrookhaven National Laboratory, New York, USA. *Correspondence e-mail: ulrike.boesenberg@xfel.eu

The high brilliance of third-generation synchrotron sources increases the demand for faster detectors to utilize the available flux. The Maia detector is an advanced imaging scheme for energy-dispersive detection realising dwell times per image-pixel as low as 50 μs and count rates higher than $10 \times 10^6 \text{ s}^{-1}$. In this article the integration of such a Maia detector in the Microprobe setup of beamline P06 at the storage ring PETRA III at the Deutsches Elektronen-Synchrotron (DESY) in Hamburg, Germany, is described. The analytical performance of the complete system in terms of rate-dependent energy resolution, scanning-speed-dependent spatial resolution and lower limits of detection is characterized. The potential of the Maia-based setup is demonstrated by key applications from materials science and chemistry, as well as environmental science with geological applications and biological questions that have been investigated at the P06 beamline.

1. Introduction

Spatially resolved scanning X-ray fluorescence spectroscopy (XRF) utilizing full spectra finds application in a wide range of research fields including biology, geology, catalysis, cultural heritage and materials science where samples often contain elements over a wide concentration range. Depending on the samples or application, sometimes small changes in the bulk composition need to be measured, or in other cases concentrations are only at trace levels. This poses high demands on the dynamic range of the detector as well as the spectral analysis procedure. In general, we would like to capture details with highest spatial resolution while placing them within a larger hierarchical spatial context of chemical and/or textural features, and therefore analysis and characterization of structures from sub- μm to cm within a single experiment is desirable.

The high brilliance of third-generation synchrotron sources enables very short XRF exposure times with adequate signal-to-noise ratio. This increases the demand for fast detectors to cope with and utilize the high available flux. A significant step in minimizing scanning times has been the implementation of so-called 'on-the-fly' scanning or sweep scans, where the stages are in continuous motion. This reduces the experimental overhead by eliminating motor settling times. Temporal resolution down to milliseconds has been achieved for a setup with a four-channel silicon drift detector (Vortex) in combination with xMAP readout electronics (XIA LLC, USA)



(Chen *et al.*, 2014). Recent developments to cope with count rates of a few 10^6 s^{-1} using advanced readout algorithms were achieved by Quantum Detectors Inc. (Nazaretski *et al.*, 2015) and XIA Ltd and Southern Innovation (Scoullar *et al.*, 2011) for single- and multi-channel detectors.

A different approach is the Maia detector, an advanced energy-dispersive detection imaging system which was developed by a collaboration between Brookhaven National Laboratory and the Commonwealth Scientific and Industrial Research Organisation (CSIRO) (Ryan *et al.*, 2010, 2013). To cope with the high photon flux, the sensor and front-end electronics are segmented into 384 individual channels in order to minimize the serious photon pileup artefacts, significant dead-time, or degraded energy resolution likely in single-channel detectors at such rates. Image-pixel dwell times as low as $50 \mu\text{s}$ and count rates higher than $10 \times 10^6 \text{ s}^{-1}$ can be realised with this detector. In order to handle the high data flux, event-mode data collection with real-time processing was chosen. For this, the Maia detector uses a field programmable gate array (FPGA) processor which provides the platform in which established techniques for real-time spectral deconvolution can be applied, particularly computation of deconvoluted element images for display in real time (Kirkham *et al.*, 2010). The photon data are directly linked to the encoder-readout of the continuously moving sample stages and for analysis the corresponding software package *GeoPIXE* is used (Ryan *et al.*, 1990, 2010). With this setup, images with more than 10×10^6 pixels can be collected on practical time scales (3–10 h), which visualize elemental distribution over roughly four orders of magnitude in space, *i.e.* over square centimeters with (sub-)micrometer resolution (Dyl *et al.*, 2014; Fisher *et al.*, 2015). The first prototypes of 96-element and 384-element detectors were successfully implemented at the XFM beamline of the Australian Synchrotron, Melbourne, Australia (Paterson *et al.*, 2011), at CHESS at Cornell University, Ithaca, NY, USA, and at the NSLS at Brookhaven National Laboratory, NY, USA (Ryan *et al.*, 2009).

The detector has a critical influence on the minimal spatial resolution and lower detection limits for samples with non-negligible thickness (Sun *et al.*, 2015). In scanning XRF, the achievable spatial resolution is determined by the beam focal size and, for samples with non-negligible thickness, the detector-to-sample geometry. Measuring in an experimental geometry where the incident beam is normal to the sample surface, in contrast to the traditional geometry with sample at 45° and the detector at 90° , was proven to be beneficial in terms of spatial resolution. On the other hand, in 90° detector geometry the spectral peak-to-background ratio is better than in backscattering geometry. However, typically a larger solid angle can more than compensate for the poorer spectral peak-to-background ratio (Sun *et al.*, 2015). The Maia detector is mounted in annular geometry with a 384-element array of planar silicon detectors which creates a large-acceptance solid angle of 1.3 sr (Ryan *et al.*, 2010, 2014).

In this article we describe the integration of such a Maia detector in the Hard X-ray Micro/Nano-Probe beamline P06 at the storage ring PETRA III at the Deutsches Elektronen-

Synchrotron (DESY) in Hamburg, Germany (Schroer *et al.*, 2010). We provide information on the detector performance such as energy resolution and achieved spatial resolution as a function of dwell time for the given beamline optics. Further, we give a first overview of the wide range of applications from materials science and chemistry, as well as environmental science with geological applications and biological questions that have been investigated at this beamline. As an upgraded version, a Maia 384C detector is currently installed at the P06 end-station, and we reference the new detector properties where possible.

2. Experimental setup

2.1. Beamline setup

The undulator beamline P06 is equipped with a cryogenically cooled double-crystal monochromator with Si(111) crystals and a Si(111) channel-cut. The incident energy range for experiments with the Maia detector is limited between 5 and 19.5 keV, the upper limit given by the Mo flight-tube and mask of the detector. An overview of the Microprobe setup is given in Fig. 1 [diagram in Fig. 1(a) and photograph in Fig. 1(b)]. Fig. 1(c) shows a detailed view of the functional parts inside the Maia detector (1). The beam is focused to approximately $450 \text{ nm} \times 450 \text{ nm}$ (horizontal \times vertical) using a Rh-coated Kirkpatrick–Baez (KB) mirror optic (6) yielding a flux in the focused beam of $\sim 10^{10}$ photons s^{-1} with a focal distance of 250 mm from the center of the second KB mirror. The beam size is determined as the FWHM of the first derivative of an edge scan over a $50 \mu\text{m}$ Au wire in the horizontal and vertical direction. Details of the setup of the beamline are given by Schroer *et al.* (2010). Accurate positioning and motion control of the sample is achieved by an encoder-controlled stage system (5) (Micos GmbH) with a LMS-230 linear motor stage in the horizontal direction providing a 50 mm travel range with 20 nm precision in closed-loop operation and a NPE-200 vertical stage with 13 mm travel range with 40 nm precision. Precise rotational movement is provided by a UPR-270-AIR air-bearing stage (eccentricity $\pm 0.07 \mu\text{m}$ and wobble $1.25 \mu\text{rad}$) and 0.0005° bi-directional repeatability. The incremental encoder signals from the sample stages are split at the SMC Hydra motion controller, digitized in interpolation units (GEMAC GmbH, Germany) if applicable and then fed directly into the Maia control unit to ensure accurate correlation between detector signal and position without affecting the standard motion control of the stages. A digital in-line optical microscope (4) is used to align the sample to the focus of the beam. Incident and transmitted flux were measured using an ionization chamber (7) and a photodiode (3), respectively. The ionization chamber is positioned between the slit system and KB system. The flux signals are amplified using a current amplifier (Keithley 428) and then fed directly into the Maia controller through a voltage-to-frequency converter. Therefore all data can be directly normalized for fluctuations in flux, dwell time, dead-time, stage acceleration and pile-up. For flat-field applications and

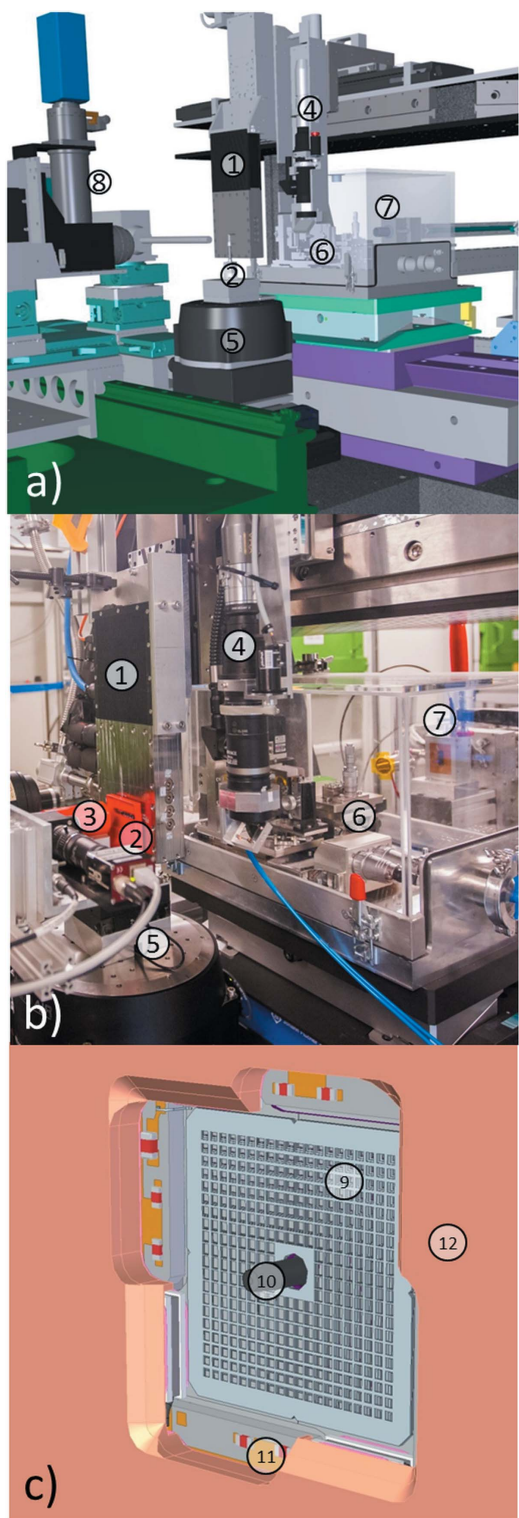


Figure 1
 (a, b) Experimental setup at the Microprobe at beamline P06, DESY, Hamburg. (a) Schematic sketch and (b) photographic image with (1) Maia detector, (2) sample and sample mount, (3) beam stop and photodiode, (4) optical microscope, (5) sample stages (x, y, z and rotation), (6) KB mirror system, (7) ionization chamber, (8) X-ray CCD camera PCO4000. (c) Sketch of the inside view of the Maia detector with the sample position approximately 10 mm from the detector array, with (9) 384-element 20 mm × 20 mm monolithic Si detector array, (10) Mo incident beam tube, (11) Peltier cooling elements, (12) Cu cooling/support block.

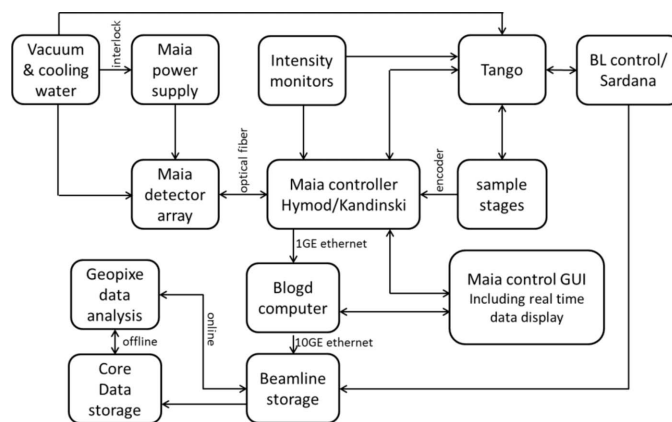


Figure 2
 Schematics of the information and media flow of the Maia detector at P06, DESY.

beam alignment a high-resolution cooled digital camera is available (8).

The Tango (Götz *et al.*, 2003) control system is used by all instrumentation at P06 and direct motion of the stages using dedicated Sardana (Reszela *et al.*, 2014) scan macros written in the Python programming language. The scan parameters are passed to the scan macros through a simple XML file, which can also be edited in a standard text editor and allows queueing of multiple samples on the same sample holder through the Taurus Macro GUI (Pascual-Izarra *et al.*, 2015) for running Sardana macros. The Maia control tool, part of the *GeoPIXE* software package, is used to monitor the scan, including online evaluation of the real-time spectrum deconvolution for imaging, and can be used for selection of regions of interest for subsequent scans from an overview scan, or for fast sample alignment (*i.e.* in case of tomography). A Tango server was written for the Maia detector to interface a subset of its native control parameters into the Tango environment, and is used for both the scan scripts and for manual intervention, using standard Tango tools like ATK. A sketch outlining the information and material flow can be found in Fig. 2.

2.2. Maia detector

The Maia detector has been well described elsewhere (Kirkham *et al.*, 2010; Ryan *et al.*, 2010, 2013, 2014; Siddons *et al.*, 2014). It is of annular type, designed for measurement in backscatter geometry. The detector sensor is a 500 μm Si monolithic array of 384 1 mm² diodes [(9) in Fig. 1(c)]. The incident beam passes through the centre of the detector *via* a Mo flight tube (10), and a further Mo mask covers the array to prevent charge-sharing between individual detector channels. A target-to-detector chip distance (2) of 10 mm provides a total solid angle of 1.3 sr, which results in a sample-to-housing distance of 1.6 mm (Ryan *et al.*, 2010, 2014). Larger sample distances can be used at the expense of sensitivity.

The detector analogue signal-processing chain is conventional in type but integrated in custom Application Specific

Integrated Circuits (ASICs) to permit the large number of individual channels in a small space. Photon events are digitized in the detector head, packaged in a small FPGA and transmitted through an optic fiber to a CSIRO Hymod FPGA-based data processing computer, which merges sample stage encoder events and performs the real-time elemental deconvolution. This is capable of an event rate of up to $50 \times 10^6 \text{ s}^{-1}$. Both the ‘raw’ photon and stage motion event data, optionally filtered to reduce count rates from many abundant events (*e.g.* scatter), and the per-pixel deconvoluted elemental concentration vector data are handled by a separate binary logger (blogd) computer to be fed into the fast beamline storage, before being automatically copied to the DESY GPFS Core storage system.

2.3. Spatial resolution

The dependence of the spatial resolution on the scanning speed of the system was tested with a ‘Siemens star’ NTT-AT resolution test pattern (model ATN/XRESO-50HC, with 500 nm materials thickness) with data acquired at an incident photon energy of 11.5 keV. The Ta-fluorescence map collected with 100 nm pixel size and 100 ms dwell time is shown in Fig. 3(a). Spatial frequency analysis was performed on a series of images with varying dwell times and pixel size. To avoid edge effects a Kaiser–Bessel function was applied as a filter with $\beta = 2$. Fig. 3(b) shows the average power spectrum of the image in Fig. 3(a) and indicates 225 nm half-period structure width, according to the criterion defined by Modregger *et al.* (2007). This is consistent with visual inspection of the images, where 200 nm pattern and spaces can be resolved. The correlation between dwell time and resolved half-period structure width can be found in Table 1. Shorter dwell times make the test pattern image appear gradually more grainy, which is probably caused by vibrations of sample and beam position.

2.4. Energy resolution and sensitivity

Energy resolution and lower detection limits were determined using a homogeneous multi-element thin-film standard

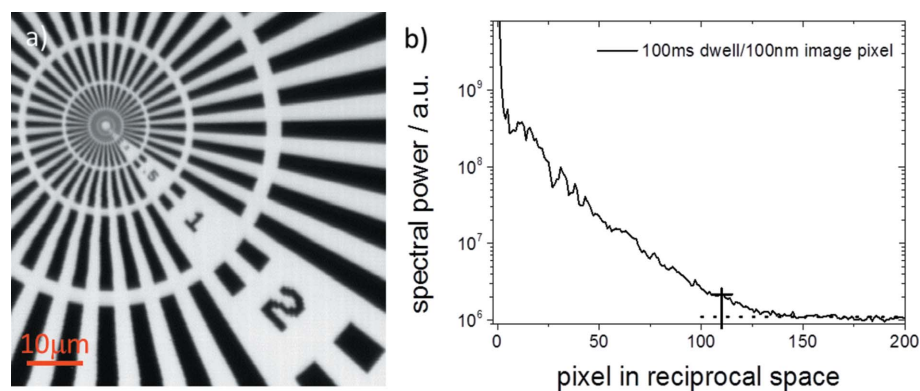


Figure 3
(a) Ta-fluorescence map of a NTT-AT resolution test pattern (dwell time 100 ms per pixel, $100 \text{ nm} \times 100 \text{ nm}$ pixel size) and (b) the corresponding average power spectrum. A Kaiser–Bessel function was applied as a filter with $\beta = 2$. A resolution of 225 nm half-period structures was determined.

Table 1

Spatial resolution with cutoff frequency and half-period structure width for dwell times between 0.1 and 100 ms determined by spatial frequency analysis.

Dwell (ms)	Pixel size (nm)	Half-period structure (nm)
0.1	100×100	354
0.3	100×100	340
1	100×100	322
10	100×100	267
100	100×100	225

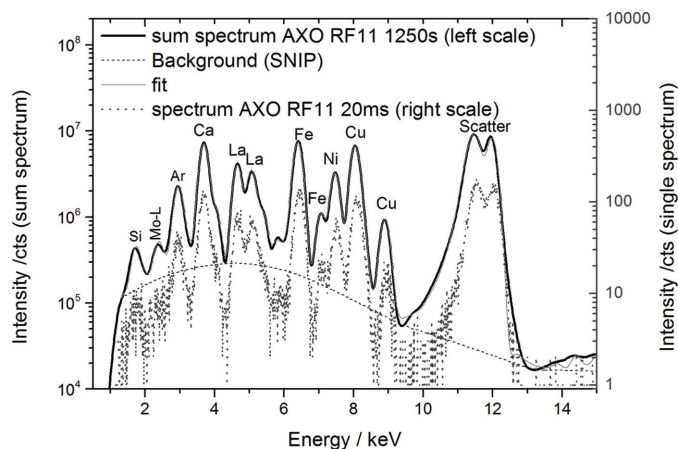


Figure 4

XRF sum spectrum of thin-film standard RF11 prepared by AXO Dresden GmbH measured over an area of $1 \text{ mm} \times 1 \text{ mm}$ with $4 \mu\text{m}$ pixel size and a dwell time of 20 ms per pixel at an incident energy of 12 keV, thus a total of 1250 s. The gray dotted line shows a full XRF spectrum collected at a single image pixel for 20 ms.

R11 prepared by AXO Dresden GmbH. The sample was scanned at a primary energy of 12 keV with a pixel size of $4 \mu\text{m}$ and a dwell time of 20 ms per pixel. All data were normalized to the incident flux rate I_0 recorded by an ionization chamber which is positioned in the primary beam. Fig. 4 shows the sum spectrum of area $1 \text{ mm} \times 1 \text{ mm}$ and thus a total exposure time of 1250 s.

The lower limit of detection (LLD) for element concentrations was determined using the *GeoPIXE* software package with

$$\text{LLD} = 3.29 \frac{\sqrt{I_{\text{back}}}}{I_{\text{signal}}} c \frac{1}{\sqrt{t}}, \quad (1)$$

where c corresponds to the concentration of the element in the standard, I_{back} the net count-rate of the background signal, I_{signal} the net count-rate of the signal, 3.29 corresponding to a confidence level of 99% in Poisson statistics and t is the dwell time. The results for the LLD are summarized in Table 2.

With a low-energy cutoff in the spectra of approximately 1.4 keV we observed the Si $K\alpha$ line at 1.7 keV. Low

Table 2

Lower limits of detection determined at 12 keV using the multi-element thin-film standard RF11 prepared by AXO Dresden GmbH; the corresponding sum spectrum over an area of approximately 1 mm × 1 mm is shown in Fig. 4.

Element	Nominal concentration (ng mm ⁻²)	LLD for 1 s (ng mm ⁻²)	LLD for 1 ms (ng mm ⁻²)	LLD for 1 ms [fg spot ⁻¹ (0.45 μm × 0.45 μm)]
La L	117.0 ± 10.9	0.424	13.416	2.717
Cu K	22.1 ± 1.9	0.017	0.537	0.109
Fe K	39.6 ± 4.4	0.035	1.118	0.226
Ca K	166.1 ± 7.2	0.350	11.069	2.241

energy sensitivity is especially interesting for biological applications because it should allow us to detect elements with low atomic numbers such as S and P. A reduction of air scattering and Ar fluorescence will be achieved by an improved beam stop in future measurements and/or a He-flushed enclosure. Contribution of stainless steel elements (Cr, Fe, Ni) inherent to the beamline components were observed to interfere with detection of ultra-traces. The detection in backscatter geometry favors the contribution of the scatter to the detected signal, thus raising the detection limits in strongly scattering samples.

Dedicated experiments using a Fe⁵⁵ source showed an energy resolution of 255 eV FWHM with 71% of the 384 detector elements showing an energy resolution better than 260 eV for the Mn Kα line. Typical count rates per detector element were around 1000–2000 s⁻¹ with an overall count rate of the detector array of approximately 550000 s⁻¹. Fig. 5(a) shows the spatial (gray scale) and statistic (blue) distribution of the energy resolution in the 384C detector.

The energy resolution of the detector as a function of count rate was determined for two shaping times, 2 and 4 μs, and is shown in Fig. 5(b). For count rates below approximately 1 × 10⁶ s⁻¹ a better energy resolution can be obtained with the longer shaping time (4 μs in this case) while for count rates higher than 1 × 10⁶ s⁻¹ shorter shaping time (2 μs) yields less peak broadening.

3. Examples and applications

3.1. Two-dimensional scans

Typical applications of two-dimensional XRF analyses are biological samples, geological samples or samples from cultural heritage studies. In general, details with highest spatial resolution shall be captured while placing them within a larger hierarchical spatial context of chemical and/or textural features, and therefore analysis and characterization of structures from sub-micrometer to centimeter within a single experiment is desirable. The Maia detector facilitates the measurement of megapixel arrays in reasonable times of hours.

3.2. Biological samples

Metals in biological systems are present usually only in trace and ultra-trace amounts, but XRF spectroscopy is an

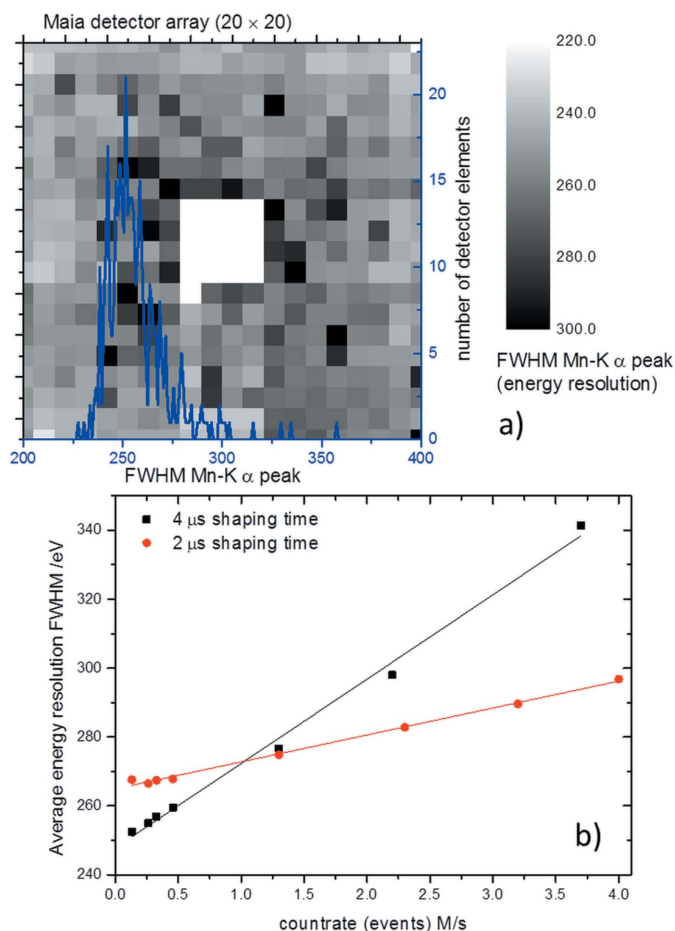


Figure 5 (a) Spatial (gray scale) and statistic (blue) distribution of the energy resolution as the FWHM of the Mn Kα peak obtained with a ⁵⁵Fe source for the DESY Maia 384C7 detector. An average energy resolution of 255 eV FWHM with 71% of the 384 detector elements showing an energy resolution better than 260 eV was determined. (b) The average energy resolution of the detector shown as a function of count rate at two different preamplifier shaping times, 2 and 4 μs. These data were obtained from irradiating a thin Fe target with synchrotron radiation of 11 keV.

ideal tool to detect them (de Jonge & Vogt, 2010). Instrumental development progresses quickly and pushes the limits of XRF microscopy in whole cell and tissue analysis continuously (Chen *et al.*, 2014; de Jonge *et al.*, 2014). In many cases, correlation of multi-element distribution is essential to understand underlying mechanisms of uptake or functionality of specific elements.

Here we show as an example a study of Bohic *et al.* (Inserm, France) investigating cartilage maturation. Coarse overview scans were performed to define the region of interest at the interface between bone and collagen, where higher-resolution scans (1 μm step size) with dwell times of 50–70 ms per point were performed. Fig. 6 illustrates the elemental distribution of S, Zn and Ca of the control sample (Fig. 6a) and after different treatments. Fig. 6(b) refers to control growth-factor-treated immature bovine cartilage that has been shown to display properties correlating with a convergence to the mature cartilage phenotype (Khan *et al.*, 2013) and Fig. 6(c) shows immature bovine cartilage treated with platelet-rich plasma.

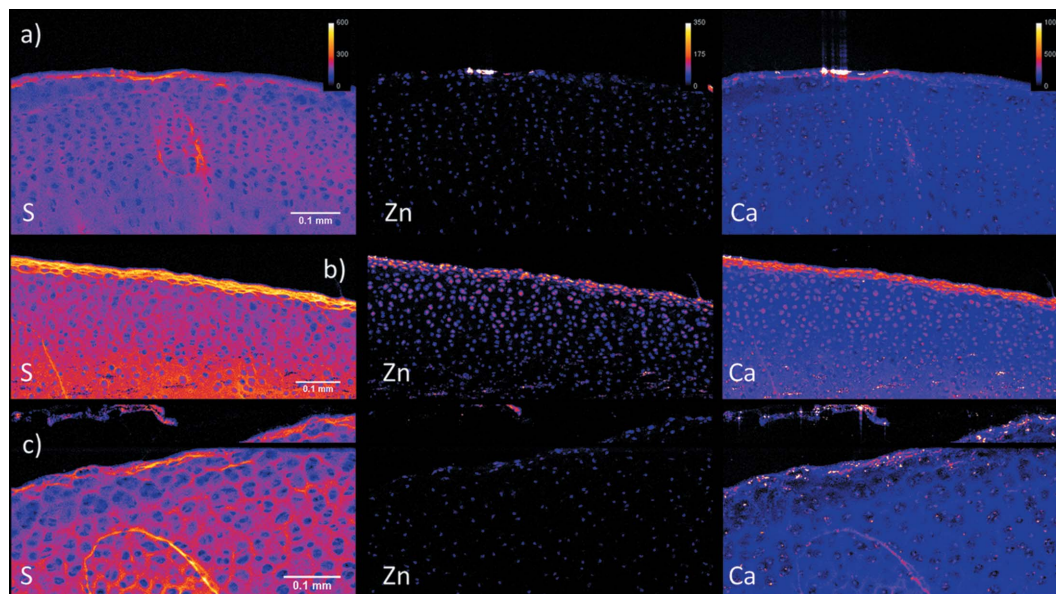


Figure 6

Two-dimensional micro-XRF image of a 20 μm cryostat section of cartilage samples. (a) Control immature bovine cartilage explant cultured for 21 days in serum-free culture medium (Khan *et al.*, 2013). (b) Similar cultured cartilage explants treated with growth factors. (c) Platelet-rich plasma treated. Areas of about $700\ \mu\text{m} \times 400\ \mu\text{m}$ were scanned with 1 μm step size and dwell times of 50–70 ms. The small black gap in (c) is due to a lack of data because of a short beam dump of the synchrotron storage ring during the acquisition period. For each element, all samples are on the same intensity scale.

Clear differences can be seen in these elemental distributions. Sulfur appears to be representative of the cartilage matrix. This agrees with histological observation of increased fibril density at the surface in growth-factor-treated surface cartilage compared with control and generally much finer structure within the cartilage matrix. Zinc is found to be associated with chondrocyte with noticeable difference again between growth-factor-treated immature cartilage (density of chondrocytes and associated zinc content seems to be higher), and control calcium seems to be associated with the cartilage matrix.

The large contribution from the scatter peak challenges the detection of trace elements or low concentrations typical for biological samples. Deviations from ideal detection schemes challenge the signal-to-scatter ratio, as is the case for all detectors, but especially pronounced in annular geometry and using large solid angle, where the intrinsic scattering is higher in comparison with a 90° geometry and small solid angle for horizontally polarized radiation (Vincze *et al.*, 1999). However, given the large solid angle of the Maia detector the advantage of the 90° geometry tends to be diluted with only a marginal penalty of a factor of three in the annular geometry (Ryan *et al.*, 2014). To measure frozen hydrated biological specimens, which can better retain their natural structure and show reduced beam damage, a cryo-stream has been mounted to keep the samples in the frozen state. However, it should be noted that a deviation from optimum sample thickness (5–10 μm for submicrometer spatial resolution) increases the incoherent scatter contribution further. Often, sturdier samples are used to withstand the flow of the cryo-stream better. If necessary, the increased incoherent scatter contribution from air scattering could be addressed by a smart combination of beam-stop and He-environment. In addition,

the authors would like to point out the availability of a cryo-chamber designed for measurements of frozen hydrated samples with a fluorescence detector in 115° geometry and a full-field detection scheme in transmission geometry at P06.

3.3. Geological samples

The second example refers to measurements of trace element concentrations of transition metals in geological samples such as a mineral thin section. Many geological applications represent fine-detail problems that can be described as ‘needles in a haystack’. Examples include rare gold particles sought in studies of ore genesis (Fisher *et al.*, 2015; Barnes *et al.*, 2016), rare resilient platinum group minerals that may survive in the Earth’s mantle for billions of years (Fonseca *et al.*, 2012), elusive gold precipitates in plants growing over ore deposits (Lintern *et al.*, 2013) or rare pre-solar condensates that may provide clues to early solar system formation (Bland *et al.*, 2005) if they can be identified. However, these objects may occur only at average concentrations of a few parts per billion, concentrated in a few sub-micrometer phases, located at unknown depths below the sample surface. X-ray fluorescence microscopy is ideal for this type of analysis as it can detect and image a sub-micrometer particle at tens of micrometers depth within a section. If we concentrate on the goal of maximizing information content within the scale of geological samples presented for X-ray fluorescence mapping analysis (*e.g.* in the form of mineralogical thin-sections) then the textural clues are contained within spatial scales from a few centimeters down to the focused X-ray beam size of $<1\ \mu\text{m}$ (Dyl *et al.*, 2014; Ryan *et al.*, 2014; Fisher *et al.*, 2015).

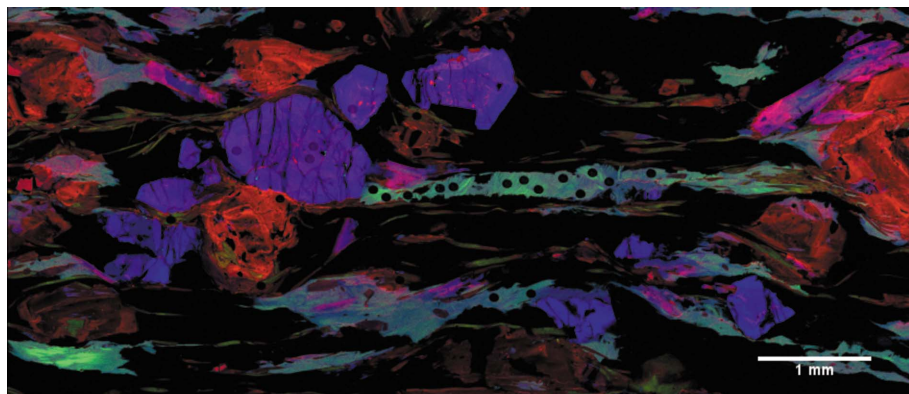


Figure 7

Two-dimensional micro-XRF RGB image of a polished thin-section from the West African Craton, with Cr (red), Ni (green) and Fe (blue). The scanned area was approximately $8\text{ mm} \times 3.4\text{ mm}$ with $600\text{ nm} \times 600\text{ nm}$ pixel size and a dwell of 0.5 ms per pixel (De Andrade *et al.*, 2014).

Such chemical maps provide input for calculations of the conditions for crystallization of the rock-forming minerals and can thus provide insight into geological processes. Fig. 7 shows an image from a study performed on West African Craton minerals, which is mainly composed of chlorite and phengite phyllosilicates (Ganne *et al.*, 2012; De Andrade *et al.*, 2014). Analysis of the element images enabled rare high-pressure relic minerals to be located and re-analyzed later with precise point analyses. The pressure–temperature conditions of crystallization calculated from these analyses are typical of modern subduction zones, which revises the onset of modern-style plate tectonics to 2.15 Gy (De Andrade *et al.*, 2014).

3.4. Three-dimensional datasets

The dataset can be easily expanded to higher dimensions, most commonly (i) repetitions for time-resolved studies or *operando* measurements, (ii) energy as a third dimension for chemical speciation utilizing the energy shift of an absorption edge with oxidation state and (iii) rotation for full three-dimensional tomographic imaging with elemental resolution. Obviously, combinations of all of these are possible and are limited only by the amount of available beam time. Time-resolved studies typically consist of a series of standard scans.

3.5. Energy-resolved mapping

Often not only the elemental information is crucial to understand the functionality of a specific element but also its chemical state, *i.e.* its chemical compound or oxidation state (Gräfe *et al.*, 2014). In spectro-microscopy, two-dimensional information about the distribution of chemical status, such as the oxidation state, can be obtained by measuring two-dimensional maps at multiple energies in the vicinity of an absorption edge. The process is also referred to as XANES mapping and is commonly applied in (scanning and full-field) transmission X-ray microscopy, where the transmitted signal is used rather than the X-ray fluorescence signal. Using XRF, this is achieved, in the simplest case, by collecting maps at two selected marker energies, where the difference between the

chemical states is largest (Marcus, 2010; Lühl *et al.*, 2013). Additionally, reference measurements below and above the absorption edge for background correction and normalization are mandatory. More advanced data analysis can be achieved by collecting a larger dataset with closely spaced energy points across the absorption edge, which enables more chemical components to be identified. Due to the large time required for the collection of a large number of XRF maps, this was until recently (Etschmann *et al.*, 2010) limited to selected sample spots (Denecke *et al.*, 2013; Marcus & Lam, 2014), small areas or transmission X-ray microscopy (Lawrence *et al.*, 2003;

Guttmann *et al.*, 2011; Meirer *et al.*, 2011; Boesenberg *et al.*, 2013). From these datasets, X-ray absorption spectra of single spatial pixels can be extracted and analyzed, *e.g.* with principle component analysis (PCA) or linear combination fitting of standard references.

This approach was followed using the Maia detector at P06 on a cycled $\text{LiNi}_{0.5}\text{Mn}_{1.5}\text{O}_4$ electrode for Li-ion batteries by measuring 53 two-dimensional datasets at selected energies in the vicinity of the Ni *K*-edge (8333 eV) (Boesenberg *et al.*, 2015), which is the redox active element in the investigated material. Spectral deconvolution and image frames were generated using the *GeoPIXE* software (Ryan *et al.*, 2010) using a dynamic analysis method in which the energy of the deconvoluted scattering lines tracks the changing beam energy. Energy stacking, alignment and linear combination fitting of the single-pixel XANES spectra were performed using the *TXMwizard* software (Liu *et al.*, 2012a,b). Fig. 8(a) shows an RGB image of a large (about $1\text{ mm} \times 5\text{ mm}$) region of a $\text{LiNi}_{0.5}\text{Mn}_{1.5}\text{O}_4$ electrode charged to an intermediate voltage with Ni (red), Mn (green) and transmission (blue). The image clearly shows an inhomogeneous distribution of the transition metals caused by the cycling of the battery. The region marked by the black square was selected for XANES mapping at the Ni *K*-edge. Figs. 8(b) and 8(c) show the relative intensity maps for Mn and Ni, respectively, in this selected region measured at 8800 eV, clearly marking spots with enhanced Ni concentration. From this region, the dataset for the construction of the Ni phase map (Fig. 8d) of the oxidation state was established by collecting XANES maps. From this image stack, single-pixel XANES were extracted and each fitted with a linear combination (LC) of reference spectra. According to the fraction of the components in each pixel, a color-coded chemical phase map is drawn and shown in Fig. 8(d). The result shows a correlation between less oxidized regions and Ni hot-spots. Inhomogeneous distribution of charge can have a significant effect on the performance of the battery and lead to premature aging effects and loss in capacity (Harris & Lu, 2013). Fig. 8(e) shows selected single-pixel XANES for the marked spots in panel (d) in correlation to the

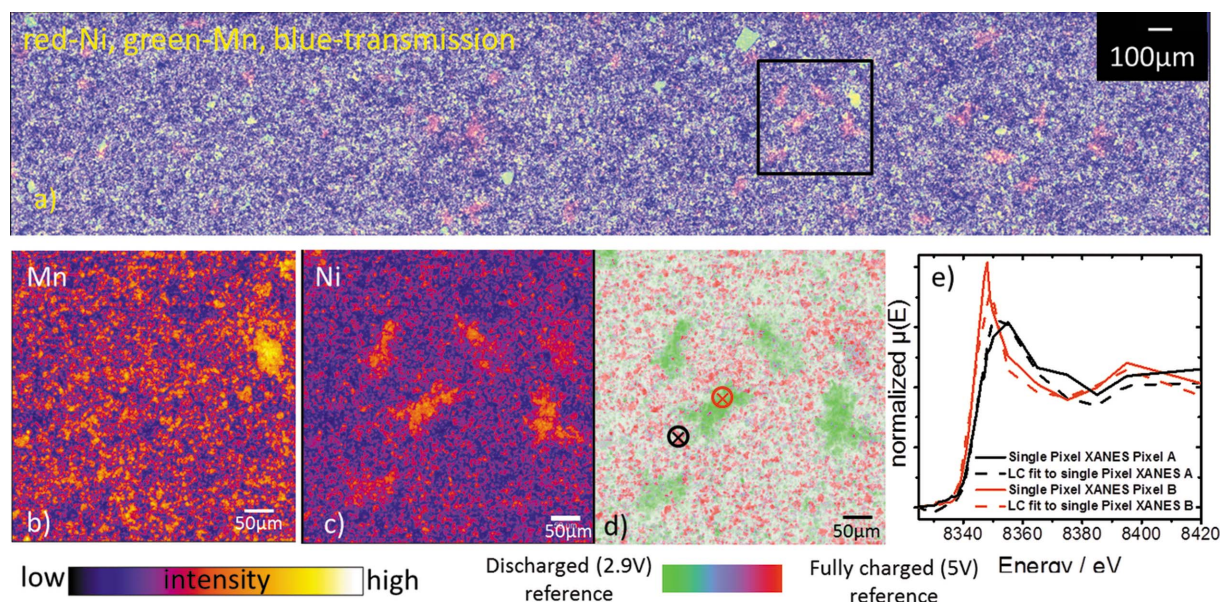


Figure 8

(a) RGB image of a large (about 1 mm × 5 mm) region of a $\text{LiNi}_{0.5}\text{Mn}_{1.5}\text{O}_4$ electrode charged to 4.783 V with Ni (red), Mn (green) and transmission (blue). (b, c) Relative intensity maps of Mn and Ni from the selected region marked in (a), 0.5 mm × 0.5 mm in size, selected for XANES mapping. (d) Phase distribution of the Ni oxidation state in the selected region obtained by linear combination (LC) fitting. (e) Single-pixel XANES at the selected spots marked in (d) and the correlated LC fit. Adapted from Boesenberg *et al.* (2015). Reprinted with permission from Boesenberg *et al.* (2015). Copyright 2015 American Chemical Society.

linear combination fitting of these selected pixels with reference samples.

Another scientific field which was shown to benefit from large-area XRF–XANES imaging using the Maia detector is cultural heritage. An example is the work of Monico *et al.* (2015), which used XANES mapping to provide new insights into the aging processes in historical paintings.

3.6. Tomography

The common two-dimensional XRF mapping scheme is often adapted towards a tomographic measurement of a single slice (Schroer, 2001) in order to obtain information on the inner structures and elemental distributions of a specimen. Full XRF raster scanning in three dimensions is rarely applied due to the long measuring times. In contrast to confocal XRF (Fittschen & Falkenberg, 2011) or color X-ray cameras (Scharf *et al.*, 2011; Garrevoet *et al.*, 2014; Radtke *et al.*, 2014), the best achievable resolution is limited by the beam size rather than capillary detector optics ($\geq 10 \mu\text{m}$).

The long exposure times for full three-dimensional high-resolution (sub-micrometer) data acquisition with conventional XRF detectors in the 30 h range for micrometer-sized samples impose a number of technical issues such as beam damage, increased drifts in sample position and simply time consumption. Three-dimensional nanoscale resolution (200 nm) of XRF tomography was achieved at the European Synchrotron Radiation Facility (ESRF) on cometary matter using two opposing (180° shifted) VORTEX EX detectors within 27 h (Boone *et al.*, 2014). Similarly, 400 nm-resolution tomography on biological samples was achieved at the Advanced Photon Source (APS) with a total measurement

time of 36 h (de Jonge *et al.*, 2010). A clear advantage of two-dimensional image acquisition and subsequent rotation was reported in both measurements to allow for correction of drifts/positioning errors.

At P06 both kinds of experiments, full three-dimensional XRF raster scanning and single-slice tomography, were performed using the Maia detector. The streamlined data acquisition of the Maia detector scheme in terms of (i) reduced exposure time, (ii) continuous movement of the sample stages, (iii) reduced dead-time and fast data handling and (iv) spatial resolution offer a substantial advantage, which was recently demonstrated at the Australian Synchrotron (Lombi *et al.*, 2011; Kopittke *et al.*, 2012). At the Hard X-ray Micro/Nano-Probe beamline P06, we recently acquired a full three-dimensional tomographic dataset with $500 \text{ nm} \times 500 \text{ nm}$ pixel size (two-dimensional) with 2 ms dwell time per pixel on a $\sim 50 \mu\text{m}$ -diameter catalyst particle in 360 projections within 8 h (Kalirai *et al.*, 2015). The results from these measurements are summarized in Fig. 9. The elastic signal was used to identify the particle matrix and assess its pore structure, with large pores greater than 500 nm. For particles taken at the end of their catalytic life, Ni and Fe fluorescence signals were found to be increased at the outer surface of the particles. Ni is not present in the pristine particle whereas the clay matrix also contains small amounts of Fe, suggesting accumulation of Ni as well as Fe from impurities in the feedstock. By measuring over the full 360° range, self-absorption effects could be determined. The high concentrations at the surface of the particle suggest a detrimental blocking of the pore structure, as such blocking can prevent feedstock molecules from reaching the central parts of the particle. This drastically reduces the active surface and thus decreases the efficiency of

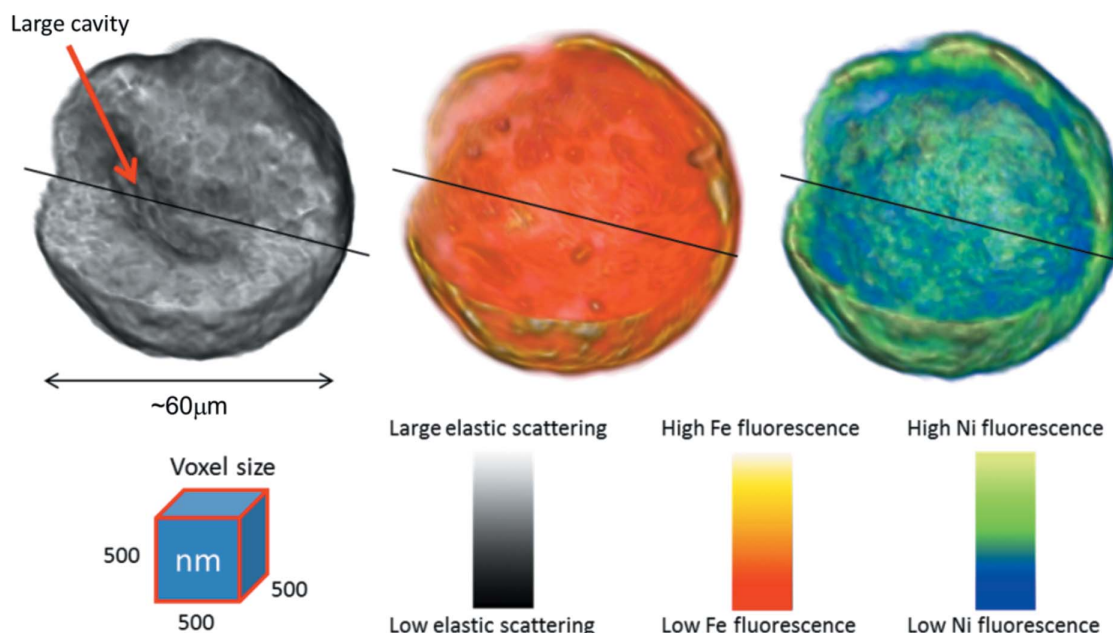


Figure 9 Reconstruction of full three-dimensional fluorescence tomography on an aged catalyst particle. In gray, the three-dimensional reconstruction of the elastic scattering contribution is shown, while red/yellow and blue/green display the three-dimensional distribution of Fe and Ni, respectively.

the catalyst. Although these measurements suffer from the mesoscale resolution of about $1\ \mu\text{m}$ in three dimensions only resolving the largest pores in the particle, the great advantage is the simultaneous detection of multiple transition metals present in a single measurement, thus allowing their precise correlation.

4. Conclusions and outlook

The Maia detector has proven to be a great asset for fast-scanning micro-XRF applications at the Microprobe at beamline P06. In particular, the fact that large sample regions can be scanned with lower resolution in a rapid preliminary pass enables reliable identification of promising regions of interest or alignment of samples for tomography. The fast-scanning schemes coupled with the rather spacious working environment invite *operando* studies on reactive media. Combined with the multilayer monochromator with 30 times higher photon flux, this should prove beneficial in terms of dwell times and even further open the door to a vast range of fast-scanning application such as *operando* measurements, larger regions of interest or tomography. However, the beam damage can be considerable and needs to be carefully evaluated for each sample matter; the large solid angle of Maia is crucial for minimizing damage. We further envision XRF coupled with diffractive techniques such as XRD, small-angle scattering or scanning coherent diffractive imaging by triggering a two-dimensional hybrid pixel detector (Eiger, Dectris AG, Switzerland) with each scanned pixel on the sample in the near future. The high sensitivity of XRF to low concentrations in combination with the short dwell times of the Maia detector opens the door for fast XANES or EXAFS measurements in

diluted samples with sub-micrometer spot size. Continuous energy scans for time-resolved XANES studies utilizing the Maia detector were successfully tested and will be reported elsewhere.

Acknowledgements

We acknowledge the work by Florian Meirer, Sam Kalirai, B. M. Weckhuysen (University of Utrecht), Ursula Fittschen (University of Hamburg, now Washington State University), Mareike Falk, Jürgen Janek (University of Gießen), Vincent De Andrade (APS), Silvain Bohic (Inserm and ESRF) and Ilyas Khan (University of Swansea) for providing the samples, participating in the experiments and the scientific discussions during the implementation of the Maia detection scheme at the Hard X-ray Microprobe beamline P06. Further we would like to acknowledge the help of André Rothkirch, Mateusz Czyzycki and Juliane Reinhardt, DESY. Parts of this research were carried out at the light source PETRA III at DESY, a member of the Helmholtz Association (HGF). Development of the Maia detector was funded in part by the National Synchrotron Light Source, a US Department of Energy (DOE) Office of Science User Facility operated for the DOE Office of Science by Brookhaven National Laboratory under Contract No. DE-AC02-98CH10886. CSIRO work took place within the CSIRO Sensors and Sensor Networks Transformational Capability Platform.

References

- Barnes, S. J., Fisher, L. A., Godel, B., Pearce, M. A., Maier, W. D., Paterson, D., Howard, D. L., Ryan, C. G. & Laird, J. S. (2016). *Contrib. Mineral. Petrol.* **171**, 23.

- Bland, P., Alard, O., Benedix, G. K., Kearsley, A. T., Menzies, O. N., Watt, L. E. & Rogers, N. W. (2005). *Proc. Natl Acad. Sci. USA*, **102**, 13755–13760.
- Boesenberg, U., Falk, M., Ryan, C. G., Kirkham, R., Menzel, M., Janek, J., Fröba, M., Falkenberg, G. & Fittschen, U. E. (2015). *Chem. Mater.* **27**, 2525–2531.
- Boesenberg, U., Meirer, F., Liu, Y., Shukla, A. K., Dell'Anna, R., Tyliszczak, T., Chen, G., Andrews, J. C., Richardson, T. J., Kostecki, R. M. & Cabana, J. (2013). *Chem. Mater.* **25**, 1664–1672.
- Boone, M. N., Garrevoet, J., Tack, P., Scharf, O., Cormode, D. P., Van Loo, D., Pauwels, E., Dierick, M., Vincze, L. & Van Hoorebeke, L. (2014). *Nucl. Instrum. Methods Phys. Res. A*, **735**, 644–648.
- Chen, S., Deng, J., Yuan, Y., Flachenecker, C., Mak, R., Hornberger, B., Jin, Q., Shu, D., Lai, B., Maser, J., Roehrig, C., Paunesku, T., Gleber, S. C., Vine, D. J., Finney, L., VonOsinski, J., Bolbat, M., Spink, I., Chen, Z., Steele, J., Trapp, D., Irwin, J., Feser, M., Snyder, E., Brister, K., Jacobsen, C., Woloschak, G. & Vogt, S. (2014). *J. Synchrotron Rad.* **21**, 66–75.
- De Andrade, V., Ganne, J., Dubacq, B., Ryan, C. G., Bourdelle, F., Plunder, A., Falkenberg, G. & Thieme, J. (2014). *J. Phys. Conf. Ser.* **499**, 012012.
- Denecke, M. A., Petersmann, T., Marsac, R., Dardenne, K., Vitova, T., Prüssmann, T., Borchert, M., Bösenberg, U., Falkenberg, G. & Wellenreuther, G. (2013). *J. Phys. Conf. Ser.* **430**, 012113.
- Dyl, K. A., Cleverley, J. S., Bland, P. A., Ryan, C. G., Fisher, L. A. & Hough, R. M. (2014). *Geochim. Cosmochim. Acta*, **134**, 100–119.
- Etschmann, B. E., Ryan, C. G., Brugger, J., Kirkham, R., Hough, R. M., Moorhead, G., Siddons, D. P., De Geronimo, G., Kuczewski, A., Dunn, P., Paterson, D., de Jonge, M. D., Howard, D. L., Davey, P. & Jensen, M. (2010). *Am. Mineral.* **95**, 884–887.
- Fisher, L. A., Fougereuse, D., Cleverley, J. S., Ryan, C. G., Micklethwaite, S., Halfpenny, A., Hough, R. M., Gee, M., Paterson, D., Howard, D. L. & Spiers, K. (2015). *Miner. Deposita*, **50**, 665–674.
- Fittschen, U. E. A. & Falkenberg, G. (2011). *Anal. Bioanal. Chem.* **400**, 1743–1750.
- Fonseca, R. O. C., Laurenz, V., Mallmann, G., Luguët, A., Hoehne, N. & Jochum, K. P. (2012). *Geochim. Cosmochim. Acta*, **87**, 227–242.
- Ganne, J., De Andrade, V., Weinberg, R. F., Vidal, O., Dubacq, B., Kagambega, N., Naba, S., Baratoux, L., Jessell, M. & Allibon, J. (2012). *Nat. Geosci.* **5**, 60–65.
- Garrevoet, J., Vekemans, B., Tack, P., De Samber, B., Schmitz, S., Brenker, F. E., Falkenberg, G. & Vincze, L. (2014). *Anal. Chem.* **86**, 11826–11832.
- Götz, A., Taurel, E., Pons, J. L., Verdier, P., Chaize, J. M., Meyer, J., Poncet, F., Heunen, G. & Götz, E. (2003). *Proceedings of the 2003 International Conference on Accelerator and Large Experimental Physics Control Systems (ICALPEPCS2003)*, Gyeongju, Korea, pp. 220–222.
- Gräfe, M., Donner, E., Collins, R. N. & Lombi, E. (2014). *Anal. Chim. Acta*, **822**, 1–22.
- Guttmann, P., Bittencourt, C., Rehbein, S., Umek, P., Ke, X., Van Tendeloo, G., Ewels, C. P. & Schneider, G. (2011). *Nat. Photon.* **6**, 25–29.
- Harris, S. J. & Lu, P. (2013). *J. Phys. Chem. C*, **117**, 6481–6492.
- Jonge, M. D. de, Holzner, C., Baines, S. B., Twining, B. S., Ignatyev, K., Diaz, J., Howard, D. L., Legnini, D., Miceli, A., McNulty, I., Jacobsen, C. J. & Vogt, S. (2010). *Proc. Natl Acad. Sci. USA*, **107**, 15676–15680.
- Jonge, M. D. de, Ryan, C. G. & Jacobsen, C. J. (2014). *J. Synchrotron Rad.* **21**, 1031–1047.
- Jonge, M. D. de & Vogt, S. (2010). *Curr. Opin. Struct. Biol.* **20**, 606–614.
- Kalirai, S., Boesenberg, U., Falkenberg, G., Meirer, F. & Weckhuysen, B. (2015). *ChemCatChem*, **7**, 3674–3682.
- Khan, I. M., Francis, L., Theobald, P. S., Perni, S., Young, R. D., Prokopovich, P., Conlan, R. S. & Archer, C. W. (2013). *Biomaterials*, **34**, 1478–1487.
- Kirkham, R., Dunn, P., Kuczewski, A. J., Siddons, D. P., Dodanwela, R., Moorhead, G. F., Ryan, C. G., De Geronimo, G., Beuttenmuller, R., Pinelli, D., Pfeffer, M., Davey, P., Jensen, M., Paterson, D. J., de Jonge, M. D., Howard, D. L., Küsel, M., McKinlay, J., Garrett, R., Gentle, I., Nugent, K. & Wilkins, S. (2010). *AIP Conf. Proc.* **1234**, 240–243.
- Kopittke, P. M., de Jonge, M. D., Menzies, N. W., Wang, P., Donner, E., McKenna, B., Paterson, D., Howard, D. L. & Lombi, E. (2012). *Plant Physiol.* **159**, 1149–1158.
- Lawrence, J. R., Swerhone, G. D. W., Leppard, G. G., Araki, T., Zhang, X., West, M. M. & Hitchcock, A. P. (2003). *Appl. Environ. Microbiol.* **69**, 5543–5554.
- Lintern, M., Anand, R., Ryan, C. & Paterson, D. (2013). *Nat. Commun.* **4**, 2614.
- Liu, Y., Meirer, F., Wang, J., Requena, G., Williams, P., Nelson, J., Mehta, A., Andrews, J. C. & Pianetta, P. (2012a). *Anal. Bioanal. Chem.* **404**, 1297–1301.
- Liu, Y., Meirer, F., Williams, P. A., Wang, J., Andrews, J. C. & Pianetta, P. (2012b). *J. Synchrotron Rad.* **19**, 281–287.
- Lombi, E., de Jonge, M. D., Donner, E., Kopittke, P. M., Howard, D. L., Kirkham, R., Ryan, C. G. & Paterson, D. (2011). *PLoS One*, **6**, e20626.
- Lühl, L., Mantouvalou, I., Schaumann, I., Vogt, C. & Kanngiesser, B. (2013). *Anal. Chem.* **85**, 3682–3689.
- Marcus, M. A. (2010). *TrAC Trends Anal. Chem.* **29**, 508–517.
- Marcus, M. A. & Lam, P. J. (2014). *Environ. Chem.* **11**, 10–17.
- Meirer, F., Cabana, J., Liu, Y., Mehta, A., Andrews, J. C. & Pianetta, P. (2011). *J. Synchrotron Rad.* **18**, 773–781.
- Modregger, P., Lübbert, D., Schäfer, P. & Köhler, R. (2007). *Phys. Status Solidi. (A)*, **204**, 2746–2752.
- Monico, L., Janssens, K., Alfeld, M., Cotte, M., Vanmeert, F., Ryan, C. G., Falkenberg, G., Howard, D. L., Brunetti, B. G. & Miliani, C. (2015). *J. Anal. At. Spectrom.* **30**, 613–626.
- Nazaretski, E., Lauer, K., Yan, H., Bouet, N., Zhou, J., Conley, R., Huang, X., Xu, W., Lu, M., Gofron, K., Kalbfleisch, S., Wagner, U., Rau, C. & Chu, Y. S. (2015). *J. Synchrotron Rad.* **22**, 336–341.
- Pascual-Izarra, C., Cuni, G., Falcon-Torres, C., Fernandez-Carreiras, D., Reszela, Z., Rosanes, M. & Coutinho, T. (2015). *Proceedings of the 2015 International Conference on Accelerator and Large Experimental Physics Control Systems (ICALPEPCS2015)*, Melbourne, Australia, pp. 1138–1142.
- Paterson, D., de Jonge, M. D., Howard, D. L., Lewis, W., McKinlay, J., Starritt, A., Kusel, M., Ryan, C. G., Kirkham, R., Moorhead, G., Siddons, D. P., McNulty, I., Eyberger, C. & Lai, B. (2011). *AIP Conf. Proc.* **129**, 219–222.
- Radtke, M., Buzanich, G., Curado, J., Reinholz, U., Riesemeier, H. & Scharf, O. (2014). *J. Anal. At. Spectrom.* **29**, 1339–1344.
- Reszela, Z., Cuni, G., Fernandez-Carreiras, D., Klora, J., Pascual-Izarra, C. & Coutinho, T. (2014). *Proceedings of the 10th International Workshop on Personal Computers and Particle Accelerator Controls (PCaPAC 2014)*, Karlsruhe, Germany, pp. 25–27.
- Ryan, C. G., Cousens, D. R., Sie, S. H., Griffin, W. L., Suter, G. F. & Clayton, E. (1990). *Nucl. Instrum. Methods Phys. Res. B*, **47**, 55–71.
- Ryan, C. G., Kirkham, R., Hough, R. M., Moorhead, G., Siddons, D. P., de Jonge, M. D., Paterson, D. J., De Geronimo, G., Howard, D. L. & Cleverley, J. S. (2010). *Nucl. Instrum. Methods Phys. Res. A*, **619**, 37–43.
- Ryan, C. G., Siddons, D. P., Kirkham, R., Li, Z. Y., de Jonge, M. D., Paterson, D., Cleverley, J. S., Kuczewski, A., Dunn, P. A., Jensen, M., De Geronimo, G., Howard, D. L., Godel, B., Dyl, K. A., Fisher, L. A., Hough, R. H., Barnes, S. J., Bland, P. A., Moorhead, G., James, S. A., Spiers, K. M., Falkenberg, G., Boesenberg, U. & Wellenreuther, G. (2013). *Proc. SPIE*, **8851**, 88510Q.
- Ryan, C. G., Siddons, D. P., Kirkham, R., Li, Z. Y., de Jonge, M. D., Paterson, D. J., Kuczewski, A., Howard, D. L., Dunn, P. A., Falkenberg, G., Boesenberg, U., De Geronimo, G., Fisher, L. A., Halfpenny, A., Lintern, M. J., Lombi, E., Dyl, K. A., Jensen, M.,

- Moorhead, G. F., Cleverley, J. S., Hough, R. M., Godel, B., Barnes, S. J., James, S. A., Spiers, K. M., Alfeld, M., Wellenreuther, G., Vukmanovic, Z. & Borg, S. (2014). *J. Phys. Conf. Ser.* **499**, 012002.
- Ryan, C. G., Siddons, D. P., Moorhead, G., Kirkham, R., Geronimo, G. D., Etschmann, B. E., Dragone, A., Dunn, P., Kuczewski, A., Davey, P., Jensen, M., Ablett, J. M., Kuczewski, J., Hough, R. & Paterson, D. (2009). *J. Phys. Conf. Ser.* **186**, 012013.
- Scharf, O., Ihle, S., Ordavo, I., Arkadiev, V., Bjeoumikhov, A., Bjeoumikhova, S., Buzanich, G., Gubzhokov, R., Günther, A., Hartmann, R., Kühbacher, M., Lang, M., Langhoff, N., Liebel, A., Radtke, M., Reinholz, U., Riesemeier, H., Soltau, H., Strüder, L., Thünemann, A. F. & Wedell, R. (2011). *Anal. Chem.* **83**, 2532–2538.
- Schroer, C. G. (2001). *Appl. Phys. Lett.* **79**, 1912.
- Schroer, C. G., Boye, P., Feldkamp, J. M., Patommel, J., Samberg, D., Schropp, A., Schwab, A., Stephan, S., Falkenberg, G., Wellenreuther, G. & Reimers, N. (2010). *Nucl. Instrum. Methods Phys. Res. A*, **616**, 93–97.
- Scoullar, P. A. B., McLean, C. C., Evans, R. J., Hamm, M. E. & Hamm, R. W. (2011). *AIP Conf. Proc.* pp. 270–277.
- Siddons, D. P., Kirkham, R., Ryan, C. G., De Geronimo, G., Dragone, A., Kuczewski, A. J., Li, Z. Y., Carini, G. A., Pinelli, D., Beuttenmuller, R., Elliott, D., Pfeffer, M., Tyson, T. A., Moorhead, G. F. & Dunn, P. A. (2014). *J. Phys. Conf. Ser.* **499**, 012001.
- Sun, Y., Gleber, S., Jacobsen, C., Kirz, J. & Vogt, S. (2015). *Ultramicroscopy*, **152**, 44–56.
- Vincze, L., Janssens, K., Vekemans, B. & Adams, F. (1999). *Ar. Spectrosc.* **54**, 1711–1722.